

Highly Efficient Photo-Induced Cathodic Protection of 403SS by the All-Solid-State Z-Scheme ZnS-CdS-Ag@TiO₂ Nanoheterojunctions

Yanfeng Zhu*, Yuanwei Liu, Zhongnian Yang

Department of Chemical Engineering and Safety, Binzhou University, Binzhou, Shandong 256603, PR China

*E-mail: yanfengzhu2014@163.com

Received: 10 October 2018 / *Accepted:* 9 November 2018 / *Published:* 30 November 2018

An all-solid-state Z-scheme ZnS-CdS-Ag@TiO₂ nanoheterojunction was successfully fabricated to reduce the recombination rate of photogenerated charge carriers and enhance the photocathodic protection efficiency for 403 stainless steel (SS). The results showed that the photoabsorption spectrum of the composite film was expanded into the visible light region and that the photocurrent density was remarkably enhanced. Under irradiation conditions, the composite film as a photoanode could exhibit a striking photocathodic protection performance for the 403SS. These results demonstrated that the Z-scheme system is beneficial for improving the separation of photogenerated charge carriers, thus achieving a highly enhanced photocathodic protection performance.

Keywords: Photocathodic protection; Titanium; Stainless steel; EIS; Oxide coatings

1. INTRODUCTION

Since 1972, when Fujishima and Honda demonstrated that TiO₂ semiconductor materials could split water into hydrogen [1], the photocatalytic activity of TiO₂ materials has attracted great interest in the academic world. To date, TiO₂ semiconductor materials have been widely used in photocatalysts [2], dye-sensitized solar cells [3], photocatalytic decomposition of water into hydrogen [4], and sensors [5]. In addition, some researchers have reported that the photoelectrochemical properties of TiO₂ could be applied to the cathodic protection of metals [6-8]. Compared with conventional cathodic protection, the photocathodic protection technology has no need to supply current or sacrificial anodes, and can achieve green and nonpolluting protection of metals [6]. However, there are two key drawbacks to the practical application of photocathodic protection of bare TiO₂ films. On the one hand, due to the wide band gap of TiO₂ (anatase $E_g = 3.2$ eV), it can only be excited only by UV light which only accounts for 4-5% of

the solar spectrum [9-11]. On the other hand, the high recombination rate of the photoinduced electron-hole pairs in TiO₂ will reduce the photoelectric conversion efficiency [10,12]. To address these obstacles, various modification strategies have been employed to modify TiO₂ for the purpose of improving the photoelectric conversion activity, including elemental doping [13], loading with noble metals [14], and coupling TiO₂ with narrow gap semiconductors [15].

Among the small band gap semiconductors, CdS is one of the most promising photocatalyst candidates due to its narrower band gap ($E_g=2.4$ eV), allowing for visible light absorption of the solar spectrum [16]. When CdS is combined with TiO₂, many remarkable photoelectrochemical properties can be created because the combined band-edge levels are capable of driving charge transfer under visible light irradiation. TiO₂/CdS heterojunction systems have been extensively investigated in photovoltaic [17], water-splitting [18], photocatalysis [19], and photocathodic protection [20]. However, the disadvantage of this composite system is that the redox ability of the photogenerated electrons and holes is weakened after charge transfer [21]. It is difficult for the heterojunction system to simultaneously possess high charge-separation efficiency and strong redox capability. Therefore, it is desirable to construct a new type of heterojunction system to solve the aforementioned problems.

Recently, Z-scheme photocatalytic systems (two-step photoexcitation), mimicking the natural photosynthesis processes, have been widely used [22-24]. The Z-scheme photocatalytic system consists of two photoexcitation systems (PS I and PS II), which can achieve spatial isolation of the photogenerated electrons and holes. Thus, the electron-hole recombination rate may be reduced. Among all Z-scheme systems, the all-solid-state Z-scheme system has attracted increasing attentions, owing to its much higher photocatalytic activity [25,26]. In such all-solid-state Z-schemes system, in addition to the two photoexcitation systems (PSI and PSII), there is also a constructor to serve as the electron transfer mediator, such as a noble metal or reduced graphene oxide (rGO). The insertion of a conductor between PSI and PSII forms a known ohmic contact with low contact resistance [27]. The photogenerated electrons from the conduction band of PSII can directly recombine with the photogenerated holes from the valence band of PSI through the ohmic transfer. This reduces the distance of Z-scheme electron transfer. Therefore, the all-solid-state Z-scheme system exhibits dramatically enhanced performance in photoelectric conversion activities.

Tada et al. [25] first reported an all-solid-state Z-scheme CdS-Au-TiO₂ three-component (3C) nanojunction system. The Z-scheme 3C nanojunction exhibited much higher photocatalytic activity than the single-(1C) and two-component (2C) systems. Xie et al. [28] combined the 3C system with a one-dimensional nanotube array structure. Rather et al. [29] fabricated a C₃N₄-Au-TiO₂ nanocomposite possessing outstanding performance for water splitting. So far, a number of works have reported on the application of all-solid-state Z-scheme type nanocomposites in the photoelectrolysis of water and the photocatalytic degradation of the organic pollutants. However, no report related to the all-solid-state Z-scheme type nanocomposites for photocathodic protection has been found.

In this work, an all-solid-state Z-scheme type CdS-Ag@TiO₂ nanocomposite was fabricated by pulse electrodeposition and the successive ion layer adsorption and reaction (SILAR) technique. To suppress CdS photocorrosion, a ZnS shell was provided by the SILAR method. The CdS was chosen to sensitize the TiO₂, and Ag acted as a transporter of electrons. This nanocomposite shows an impressive photocathodic protection performance for the 403 stainless steel (SS).

2. EXPERIMENTAL

2.1. Materials

All of the chemical reagents were of analytical grade and used without further purification. Pure deionized water was used throughout the preparation of all aqueous solutions. Sodium hydroxide (NaOH), silver nitrate (AgNO₃), nitric acid (HNO₃), sodium nitrate (NaNO₃), chromic nitrate (CdNO₃), zinc nitrate (ZnNO₃), and sodium sulfide (Na₂S) were purchased from Sinopharm Chemical Reagent Co. Ltd. Ti foil (99.7% purity) and 403SS were purchased from Tianjin yuanhao metal materials Co. Ltd.

2.2. Synthesis of ZnS-CdS-Ag@TiO₂

The ZnS- CdS-Ag@TiO₂ sample was prepared as follows. First, the TiO₂ nanowire (NW) films were first prepared on Ti foil by the hydrothermal method according to our previous report [30]. The Ti foil was reacted with a 10 M NaOH solution (80 mL) in a Teflon-lined stainless steel autoclave (100 mL) at 150 °C for 6 h. After the hydrothermal process, the sample was soaked in a 0.1 M HNO₃ solution for 8 h, and the samples were then annealed in a muffle furnace at 450 °C for 2 h. Second, Ag nanoparticles were deposited on the TiO₂NWs by the pulse electrodeposition method using a two-electrode system consisting of TiO₂NWs as the working electrode and a Pt foil as the counter electrode [31]. The TiO₂NW films were immersed in a 0.01 M AgNO₃ and 0.1 M NaNO₃ mixed aqueous solution. The pulse electrodeposition current was -15 mA cm² with a 0.2 s on-time and 0.3 s off-time. The number of the pulse cycles was 600. Third, CdS nanoparticles were fabricated by the SILAR method. The Ag/TiO₂ sample was alternately immersed in a 0.4 M Cd(NO₃)₂ solution and 0.1 M Na₂S solution for 1 min. Finally, a ZnS layer was assembled onto the surface of the CdS nanoparticles, in order to improve the stability of the sample. The CdS-Ag@TiO₂ film was alternately immersed in a 0.6 M Zn(NO₃)₂ solution and 0.1 M Na₂S solution for 1 min. The immersion cycle of the prepared a ZnS layer was repeated for up to 20 cycles. Following each immersion, the film was rinsed with deionized water to remove excess precursors and dried at room temperature.

2.3 Characterization

The morphologies of the as-prepared films were characterized by a field-emission scanning electron microscope (FE-SEM Hitachi S4800). The chemical composition was analyzed by energy dispersive X-ray (EDX) spectrometry. The crystallographic structure of the films was measured by an X-ray diffractometer (XRD Bruker D8 Advance) with Cu K α . The photoabsorption properties of the samples were recorded by a UV-vis-NIR spectrophotometer (Varian, Cary 5000). X-ray photoelectron spectroscopy (XPS) was carried out by an X-ray photoelectron spectrometer (Tecni G2 20) with Al K α as the X-ray source.

The photoelectrochemical performances of the as-prepared samples were measured by an Ivium (CompactStat) electrochemical workstation with a three-electrode system consisting of a photoanode as the working electrode (10 mm \times 10 mm \times 0.1 mm), a saturated calomel electrode (SCE) as the reference

electrode and a platinum wire as the counter electrode. A CEL-S500 Xe lamp was employed as the light source. The photocurrent measurement and electrochemical impedance spectroscopy (EIS) were applied at open-circuit voltage. EIS results were obtained at an AC voltage of 10 mV amplitude over the frequency range from 10^{-2} to 10^5 Hz.

The photocathodic protection properties of the as-prepared photoanode samples were measured by a homemade system according to our previous report [32]. The protected metal was 403 stainless steel (403SS 10 mm \times 10 mm \times 2 mm). The electrolyte in the photoelectrochemical cell was a mixed solution of 0.05 M Na₂S and 0.2 M NaOH, while in the corrosion cell it was 0.5 M NaCl. The two cells were connected by a salt bridge (1.0 M KCl in agar contained in a flexible glass tube). Either TiO₂ or the TiO₂ composite film (10 mm \times 10 mm \times 0.1 mm) served as a photoanode in the photoelectrochemical cell. In the corrosion cell, the 403SS, a platinum sheet and SCE served as the working electrode, counter electrode and reference electrode, respectively. The 403SS electrode was coupled to the photoanode by a Cu wire. The measurements of potential and electrochemical impedance spectroscopy (EIS) were conducted using an Ivium electrochemical measurement system. EIS results were obtained by applying an AC voltage of 10 mV amplitude over the frequency range of 10^{-2} to 10^5 Hz. The measured EIS data were fitted by ZsimpWin fitting software. All measurements were carried out at room temperature and were repeated at least three times to check the reproducibility.

3. RESULTS AND DISCUSSION

Figure 1a shows the SEM images of the TiO₂ sample prepared in 10 M NaOH solution under hydrothermal conditions for 6 h. The film possessed a porous network morphology. The magnified image shows that the network consisted of scrolled-up nanowires. As shown in Figure 1b, the typical peaks at $2\theta = 25.5^\circ$ and 48.3° indicated that the pure TiO₂ NW film crystallized in the anatase phase (JCPDS card no. 21-1272)[24]. The ZnS-CdS-Ag@TiO₂ and Ag@TiO₂ films exhibited the similar XRD patterns (not shown in Figure 1) as the pure TiO₂ film, revealing that the addition of CdS, Ag, and ZnS hardly affected the crystalline structure of TiO₂. No characteristic diffraction peaks of CdS, Ag, and ZnS are observed due to their lower content and/or high dispersion and relatively low diffraction intensity. Therefore, the EDX and XPS spectra were further measured to analyze the elemental composition of the composite films. Figure 1c presents the SEM image of the ZnS-CdS-Ag@TiO₂ film obtained after 20 cycles of CdS and 5 cycles of ZnS. It can be observed that CdS and ZnS particles were uniformly distributed on the nanowire surface. The EDX spectrum (Figure 1d) reveals that the ZnS-CdS-Ag@TiO₂ films were composed of Ti, O, Ag, Cd, Zn and S.

The XPS measurement was carried out to further determine the chemical composition and the surface states of the as-prepared samples. Figure 2a shows the high resolution XPS spectrum of Ti 2p. The Ti 2p peak was deconvoluted into two peaks at 458.7 eV (Ti 2p 3/2) and 464.4 eV (Ti 2p 1/2), representing the Ti⁴⁺ species in a tetragonal structure[18]. The O1s spectrum (Figure 2b) is slightly asymmetric. The principal peak located at 531.5 eV corresponds to Ti-O in TiO₂. The minor peak at 532.4 eV was assigned to chemical hydroxyl [33,34]. The Ag 3d 3/2 and Ag 3d 5/2 peaks are located at 373.8 and 367.8 eV, respectively, as shown in Figure 2c. Furthermore, the splitting energy of the Ag 3d

doublet is 6.0 eV, indicating the formation of metallic Ag [35]. The deconvoluted peaks of the Cd 3d 5/2 and Cd 3d 3/2 are located at 404.7 and 411.5 eV with a splitting energy of 6.8 eV, manifesting the Cd²⁺ in CdS (Figure 2d) [36]. From the Figure 2e, it can be seen that the binding energy of Zn 2p 3/2 is located at 1021.9 eV [37]. The S 2p spectrum as shown in Figure 2f, can be fitted into two individual peaks S 2p 3/2 and S 2p 1/2 at 161.2 eV and 162.3 eV, which corresponds to the S²⁻ [38]. These results further confirm that the ZnS-CdS-Ag@TiO₂ composites have been successfully fabricated.

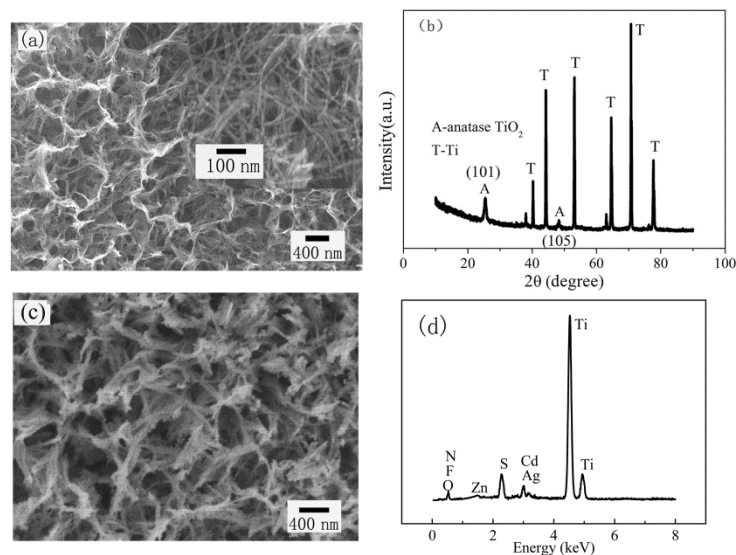


Figure 1. SEM image of (a)TiO₂ NW film and (c) ZnS-CdS-Ag@TiO₂; (b) XRD spectrum of TiO₂ NW film, (d) EDX spectrum of ZnS-CdS(20c)-Ag@TiO₂ film.

The optical properties of the as-fabricated films were further measured by UV-vis absorption spectra. Figure 3 shows the UV-vis absorption spectra of (a) pure TiO₂ and (b) ZnS-CdS(20c)-Ag@TiO₂ samples. It is obvious that the TiO₂ NW sample mainly absorbed UV light at a wavelength of approximately 370 nm. Compared with the pure TiO₂ NW film, the absorption spectrum of the ZnS-CdS(20c)-Ag@TiO₂ film extended into the visible region and the absorption edge was nearly 700 nm. For a given semiconductor, the band gap energy (E_g) can be determined using the Tauc plot by the following equation [26]:

$$\alpha h\nu = k(h\nu - E_g)^{\eta/2} \quad (1)$$

where α , h , ν and k are the absorption coefficient, Planck constant, light frequency and a constant, respectively. Furthermore, η is a constant determined by the type of optical transition of a semiconductor, which is equal to 1 for a direct-gap material, and 4 for an indirect-gap material [39,40]. According to Eq. (1), the intercept of the tangents to the plots of $(\alpha h\nu)^{2/\eta}$ vs $(h\nu)$ can be employed to determine the band gaps of TiO₂ and ZnS-CdS(20c)-Ag@TiO₂ films, due to their indirect electronic transitions. The band gap energies of the TiO₂ and ZnS-CdS(20c)-Ag@TiO₂ films were calculated to be 2.97 eV and 1.76 eV, respectively. These results indicated that the strong interactions between TiO₂, Ag and CdS in the ZnS-CdS-Ag@TiO₂ composite might result in an obvious narrowing of the band gap, which favors extension of the absorption range.

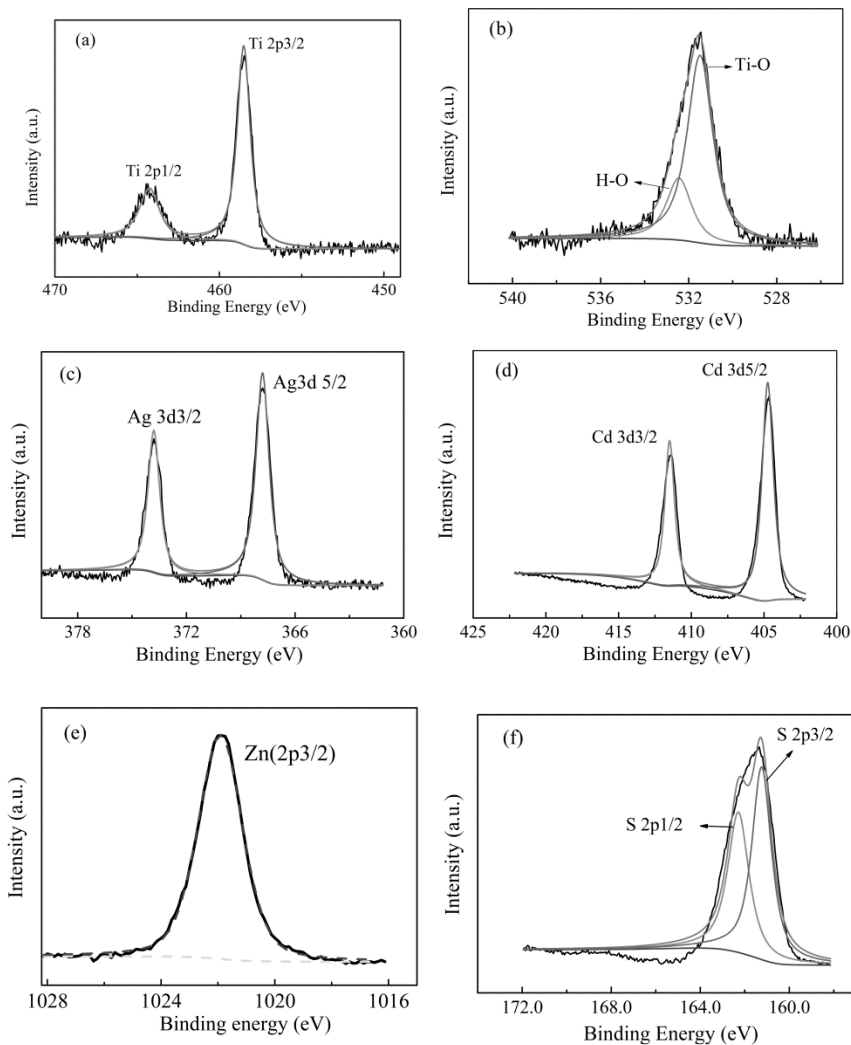


Figure 2. XPS spectra of (a) Ti 2p, (b) O 1s, (c) Ag 3d, (d) Cd 3d, (e) Zn 2p, and (f) S 2f.

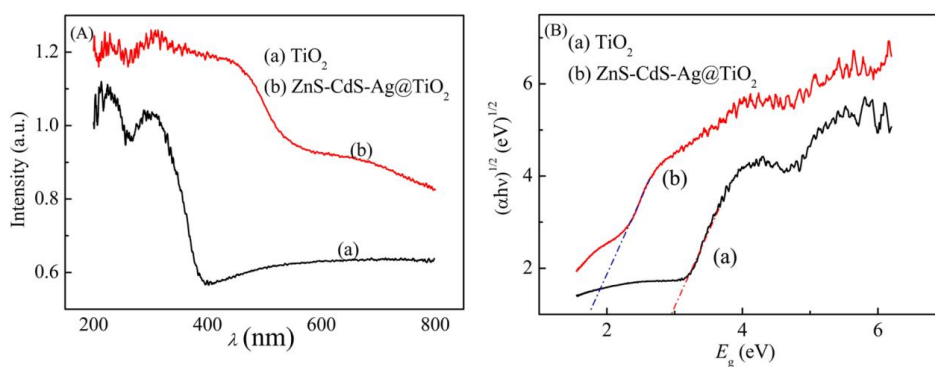


Figure 3. UV-vis absorption spectra and band gaps of different samples.

The properties of the charge transfer and photogenerated electron lifetime can be estimated by from the transient photocurrent density under illumination. The photocurrent response of different films with several on-off cycles is presented in Figure 4A. All of the samples showed a sharp anodic current

peak and a steady state current. In all cases, the modified TiO₂ electrode presented a higher photocurrent density than the pure TiO₂ electrode. Especially, the ZnS-CdS-Ag@TiO₂ electrodes (curves c, d and e) displayed a much higher photocurrent density compared with the Ag@TiO₂ electrode. The enhanced photocurrent performance may be ascribed to the high separation efficiency of photoinduced carriers via the Z-scheme form and the strong absorption in the visible light region. It is recognized that a maximum photocurrent density of 19.97 mA cm⁻² was achieved (ZnS-CdS(20c)-Ag@TiO₂). Therefore, the ZnS-CdS(20c)-Ag@TiO₂ film was the study electrode in the following paragraphs.

EIS is a powerful technology for studying the charge transfer and recombination processes at semiconductor/electrolyte interfaces [41]. Figure 4B shows an EIS plot of different semiconductor electrodes at open-circuit potential under white light irradiation conditions. It can be observed that the electrodes showed pronounced arcs in the EIS plane. The diameters of the arcs represent the reaction rate occurring at the semiconductor/electrolyte interfaces [42]. It can be observed that the EIS arc of the ZnS-CdS(20c)-Ag@TiO₂ electrode is smaller than that of the TiO₂ electrode, indicating that the rate of carrier separation and transfer in the ZnS-CdS(20c)-Ag@TiO₂ electrode was higher. This result is consistent with the transient photocurrent measurement.

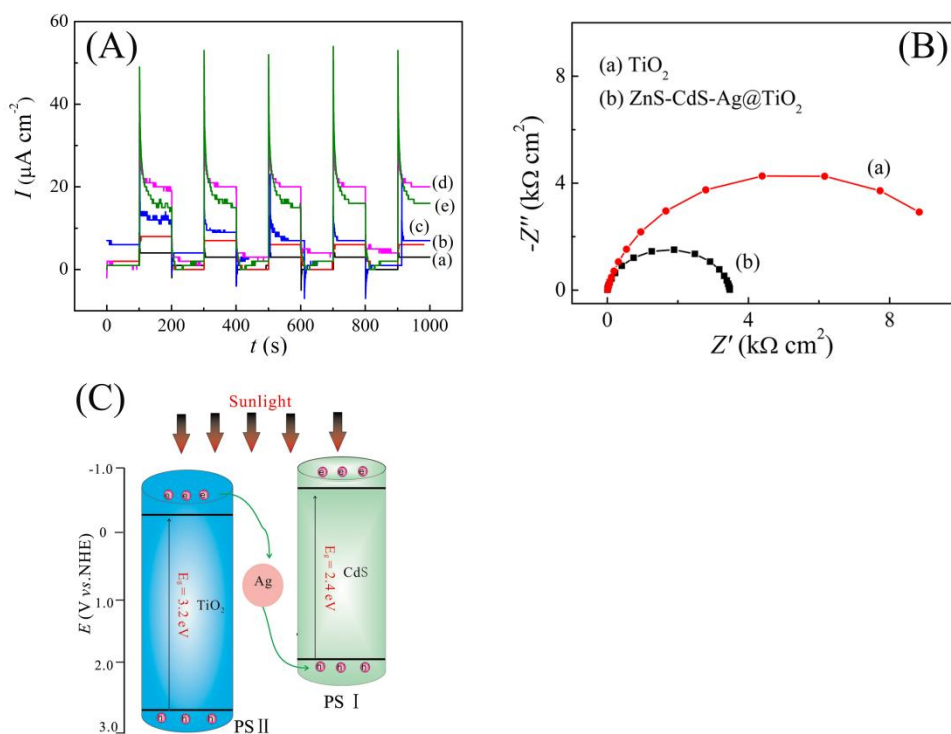


Figure 4. (A) Photocurrent responses of (a) TiO₂, (b) Ag@TiO₂, (c) ZnS-CdS(15c)-Ag@TiO₂, (d) ZnS-CdS(20c)-Ag@TiO₂, and (e) ZnS-CdS(25c)-Ag@TiO₂ photoelectrodes; (B) Nyquist plots of the as-prepared samples under white light illumination; and (C) Schematic illustration of the electron-hole separation in the ZnS-CdS-Ag@TiO₂ composites.

Figure 4C illustrates the possible principle of charge carriers in the all-solid-state Z-scheme ZnS-CdS-Ag@TiO₂ composites. In the two-component heterojunction-type system (PS I and PS II), the photoelectrons in the CB of PS I transfer to the CB of PS II, while the photoholes in the VB of PS II migrate

to the VB of PSI[43-46]. The spatial isolation of photoelectrons and photoholes can reduce the bulk electron-hole recombination. However, the redox capability of photoelectrons and photoholes is weakened after charge transfer. Therefore, it is different for the two-component heterojunction-type system to have both a high charge separation and strong redox capability. In the all-solid-state Z-scheme composite, the aforementioned problem can be solved. The path of electron transfer in the all-solid-state Z-scheme ZnS-CdS-Ag@TiO₂ composites is different from that in a two-component heterojunction-type system. Primarily, the TiO₂ (PSII) and CdS (PSI) semiconductors can generate photogenerated electron-hole pairs under simulated solar light irradiation [47]. Subsequently, photoelectrons in the CB of TiO₂ can quickly transfer to the VB of CdS through Ag, and then recombine with photoholes in the VB of CdS, forming the typical electron-transfer pathway of the Z-scheme [21,27]. Thus, photoelectrons and photoholes are accumulated in the CB of CdS and VB of TiO₂, respectively, which enabled the ZnS-CdS-Ag@TiO₂ composite film to have strong oxidation and reduction capabilities. Furthermore, the separation rate of photogenerated electron-hole pairs will be improved. Therefore, the ZnS-CdS-Ag@TiO₂ electrode exhibited higher photoelectric conversion performance.

To evaluate the photocathodic effect of the film, the potential of 403SS as a protected metal was measured. Figure 5 presents the potential response of 403SS in a 0.5 M NaCl solution coupled with different film photoanodes under intermittent illumination. It can be observed that the potential response was prompt and negatively shifted under irradiation. This was due to the transfer of the photogenerated electrons from the photoanodes to the surface of 403SS, causing the cathodic polarization of the steel, thus the metal corrosion rate is reduced [32,48-50]. The stabilized potential of 403SS coupled to the ZnS-CdS(20c)-Ag@TiO₂ and TiO₂ photoanode under illumination were recorded at approximately -1174 mV (vs.SCE) and -118 mV (vs.SCE), respectively. The results indicated that numerous photoelectrons were transferred from the ZnS-CdS(20c)-Ag@TiO₂ electrode to the steel. In addition, when the composite film continued to be illuminated after a break, the potential of 403SS again dropped to -1174 mV (vs.SCE), showing that the ZnS-CdS(20c)-Ag@TiO₂ electrode exhibited substantial activity and stability. Most importantly, after turning off the light, the potential of the steel coupled to ZnS-CdS(20c)-Ag@TiO₂ films remained lower, indicating that the ZnS-CdS(20c)-Ag@TiO₂ electrode still provides the certain cathodic protection for the steel in the dark. In other words, the ZnS-CdS(20c)-Ag@TiO₂ exhibited higher photocathodic protection than pure TiO₂ photoanode.

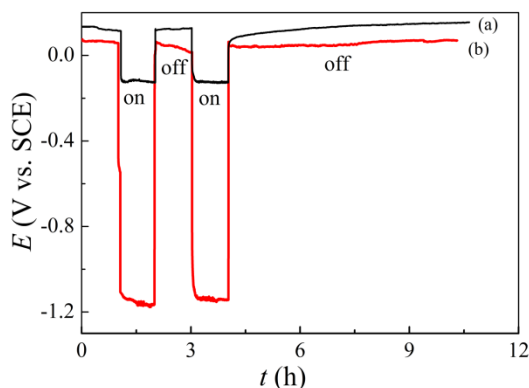


Figure 5. Time evolution of the potential of 403SS coupled to different photoanodes under illumination and dark conditions:(a) coupled to TiO₂ and(b) coupled to ZnS-CdS(20c)-Ag@TiO₂.

To further study the corrosion process of 403SS under photocathodic protection, EIS was performed under illumination. Figure 6 shows the EIS spectra of 403SS uncoupled and coupled to different photoanodes, and the equivalent circuit for modeling the EIS results. In the equivalent circuit, R_s is the solution resistance, R_{ct} is the charge-transfer resistance, and CPE is the constant phase element modeling the capacitance of the double-layer. The constant phase element can be expressed by the following equation [51]:

$$Z_{CPE} = [Y_0(j\omega)^n]^{-1} \tag{2}$$

where Y_0 represents the modulus, $j^2 = -1$ is an imaginary number, ω is the angular frequency, and n is the coefficient of diffusion, the value of n is in the range of 0 to 1. It was found that the impedance arcs in all cases were similar, but the diameter of the 403SS coupled to the photoanodes was markedly smaller. This may be due to a larger number of photogenerated electrons being transferred from the photoanode to the the surface of 403SS, leading to the cathodic current density increase for the steel [52]. According to the mechanism of cathodic protection of metals, the impressed current could make the potential of the metal sharply shift negatively and inhibit corrosion [53]. Therefore, the rate of the electrochemical dissolution reaction at the metal surface is suppressed. Additionally, the arc radius of the 403SS coupled to the ZnS-CdS(20c)-Ag@TiO₂ photoanode was obviously smaller. This may be due to the increased number of photogenerated electrons transferred from the ZnS-CdS(20c)-Ag@TiO₂ photoanode to the surface of 403SS, leading to a greater decrease in resistance. It can be inferred that the ZnS-CdS(20c)-Ag@TiO₂ composite film could provide a better photocathodic protection effect for 403SS than pure TiO₂ film.

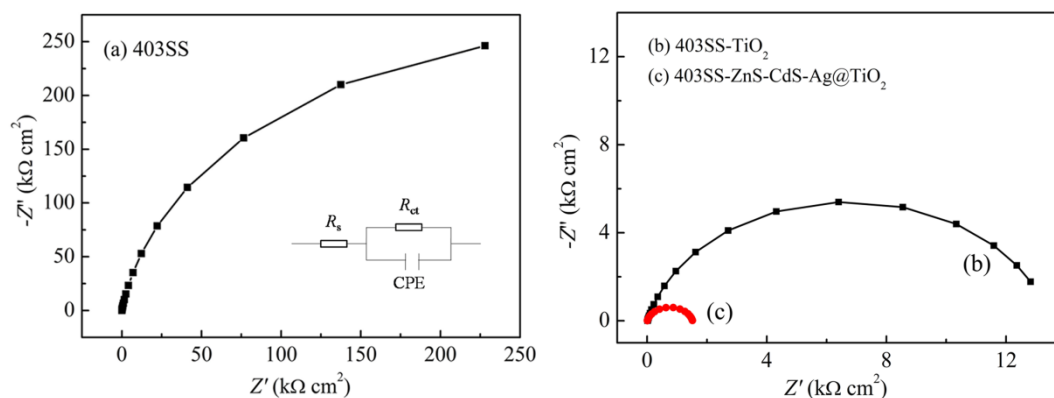


Figure 6. EIS results for 403SS under different conditions.

4. CONCLUSIONS

In this work, an all-solid-state Z-scheme ZnS-CdS-Ag@TiO₂ composite film was successfully prepared by the pulsed electrodeposition and SILAR techniques. With the modification of Ag and CdS, the photoabsorption of the composite film shifts into the visible region and the photoelectrochemical performance is enhanced markedly. The resulting ZnS-CdS(20c)-Ag@TiO₂ composite film exhibited higher photocurrent density than that of pure TiO₂ film, owing to achieving a Z-scheme charge

separation mechanisms. In addition, the composite film, as a photoanode, could make the potential of 403SS in a 0.5 M NaCl solution negatively shift markedly under irradiation, indicating highly effective photocathodic protection. Therefore, it is expected that the construction of the Z-scheme heterojunction composite film could provide some new strategies for the photocathodic protection of various kinds of metals.

ACKNOWLEDGEMENTS

This work was supported by the Natural Science Foundation of Shandong Province of China (ZR2016BP11) and A Project of Shandong Province Higher Educational Science (J16LC18).

References

1. A. Fujishima, K.Honda, *Nature*, 238 (1972), 37.
2. Q.Q. Cai, J.Y. Hu, S.Y. Lu, *J. Hazard. Mater.*, 323 (2017) 527.
3. H. Lu, W. Tian, B.K. Gu, Y.Y. Zhu, L.Li, *Small*, 13 (2017) 1701535.
4. L.J. Gao, Y.G. Li, J.B. Ren, S.F. Wang, R.N. Wang, G.S. Fu, Y. Hu, *Appl. Catal. B: Environ.*, 202 (2017) 127.
5. G.G. Bessegato, F.F. Hudari, M.V.B. Zanoni, *Electrochim. Acta*, 235 (2017) 527.
6. H. Park, W. Choi, K.Y. Kim, *Chem. Commun.*, (2001) 281.
7. Y.F. Zhu, R.G. Du, W. Chen, H.Q. Qi, *Electrochem. Commun.*, 12 (2010) 1626.
8. T.T. Zhang, Y.P. Liu, J. Liang, D.A. Wang, *Appl. Surf. Sci.*, 394 (2017) 440.
9. G.K. Mor, O.K. Varghese, M. Paulose, K. Shankar, C.A. Grimes. *Sol. Energ. Mat. Sol. C.*, 90 (2006) 2011.
10. A.L. Linsebigler, G. Lu, J.T. Yates. *Chemi. Rev.*, 95 (1995) 735.
11. Y.Y. Bu, J.P. Ao. *Green Energy Environ.*, 2 (2017) 331.
12. H. Gao, P. Zhang, J. Zhao, Y. Zhang, J. Hu, G. Shao, *Appl. Catal. B: Environ.*, 210 (2017) 297.
13. J. Li, C.J. Lin, Y.K. Lai, R.G. Du, *Surf. Coat. Tech.*, 205 (2010) 557.
14. H. Li, X.T. Wang, Q.Y. Wei, X.Q. Liu, Z.H.Qian, B.R. Hou. *Nanotechnology*, 28 (2017) 22.
15. J. Zhang, J. Hu, Y.F. Zhu, Q. Liu, H. Zhang, R.G. Du, C.J. Lin. *Corros. Sci.*, 99 (2015) 118.
16. Y. Lei, C. Yang, J. Hou, F. Wang, S. Min, X. Ma, Z. Jin, J. Xu, G. Lu, K.W. Huang, *Appl. Catal. B: Environ.*, 216 (2017) 59.
17. S.A. Pawar, D.S. Dipali, H.R. Jung, J.Y. Park, S.S. Mali, C.K. Hong, J.C. Shin, P.S. Patil, J.H. Kim, *Electrochim. Acta*, 203 (2016) 74.
18. H. Zhao, M. Wu, J. Liu, Z. Deng, Y. Li, B.L. Su, *Appl. Catal. B: Environ.*, 184 (2016), 182.
19. M.A. Mumin, G. Moula, P.A. Charpentier, *RSC Adv.*, 5 (2015) 67767.
20. J. Zhang, R.G. Du, Z.Q. Lin, Y.F. Zhu, Y. Guo, H.Q. Qi, L. Xu, C.J. Lin. *Electrochim. Acta*, 83 (2012) 59.
21. P. Zhou, J. Yu, M. Jaroniec. *Adv. Mater.*, 26 (2014) 4920.
22. J. Li, M. Zhang, X. Li, Q.Y. Li, J.J. Yang. *Appl. Catal. B: Environ.*, 22 (2017) 106.
23. Y. Sasaki, H. Kato, A. Kudo, *J. Am. Chem. Soc.*, 135 (2013) 5441.
24. X. Zeng, Z. Wang, G. Wang, T.R. Gengenbach, D.T. McCarthy, A. Deletic, J. Yu, X. Zhang, *Appl. Catal. B: Environ.*, 218 (2017) 163.
25. H. Tada, T. Mitsui, T. Kiyonaga, T. Akita, K.Tanaka, *Nat. Mater.*, 5 (2006) 782.
26. F. Wu, X. Li, W. Liu, S.Zhang, *Appl. Surf. Sci.*, 405 (2017) 60.
27. S.T. Kochuveedu, Y.H. Jang, D.H. Kim, *Chem. Soc. Rev.*, 42 (2013) 8467.
28. K.P. Xie, Q. Wu, Y.Y. Wang, W.X. Guo, M.Y. Wang, L. Sun, C.J.Lin, *Electrochem. Commun.*, 13 (2011) 1469.

29. R.A. Rather, S. Singh, B. Pal, *Appl. Catal. B: Environ.*, 213(2017) 9.
30. Y.F. Zhu, R.G. Du, J. Li, H.Q. Qi, C.J. Lin, *Acta Phys.-Chim. Sin.*, 26 (2010) 2349.
31. Y.K. Lai, H.F. Zhuang, K.P. Xie, D.G. Gong, Y.X. Tang, L. Sun, C.J. Lin, Z. Chen, *New J. Chem.*, 34 (2010) 1335.
32. Y.F. Zhu, L. Xu, J. Hu, J. Zhang, R.G. Du, C.J. Lin, *Electrochim. Acta*, 121 (2014) 361.
33. R.P. Antony, T. Mathews, S. Dash, A.K. Tyagi, B. Raj, *Mater. Chem. Phys.*, 132 (2012) 957.
34. J. Shao, W.C. Sheng, M.S. Wang, S.J. Li, J.R. Chen, Y. Zhang, S.S. Cao. *Appl. Catal. B: Environ.*, 209 (2017) 311.
35. D.H. Yu, X. Yu, C. Wang, X.C. Liu, Y. Xing, *ACS Appl. Mater. Interfaces*, 4 (2012) 2781.
36. C. Zhu, C.G. Liu, Y.J. Zhou, Y.J. Fu, S.J. Guo, H. Li, S.Q. Zhao, H. Huang, Y. Liu, Z.H. Kang, *Appl. Catal. B: Environ.*, 216 (2017) 114.
37. A. Jbeli, A.M. Ferrara, A.M.B. do Rego, S. Boufi, S. Bouattour, *Int. J. Biol. Macromol.*, 116 (2018) 1098.
38. J. Yang, J.J. Peng, R.X. Zou, F. Peng, H.J. Wang, H. Yu, J.Y. Lee, *Nanotechnology*, 19 (2008) 255603.
39. X. Li, J. Yu, J. Low, Y. Fang, J. Xiao, X. Chen, *J. Mater. Chem. A*, 3 (2015) 2485.
40. X. Li, T. Xia, C. Xu, J. Murowchick, X. Chen, *Cataly. Today*, 225 (2014) 64.
41. C.G. Morales-Guio, L. Liardet, M.T. Mayer, S.D. Tilley, M. Gratzel, X. Hu, *Angew Chem. Int. Ed. Engl.*, 54 (2015) 664.
42. J. Su, L. Zhu, G. Chen, *Appl. Catal. B: Environ.*, 186 (2016) 127.
43. L. Zheng, S. Han, H. Liu, P. Yu, X. Fang, *Small*, 12 (2016) 1527.
44. W. Sun, D. Wang, Z.U. Rahman, N. Wei, S. Chen, *J. Alloy. Compd.*, 695 (2017) 2154.
45. D.O. Scanlon, C.W. Dunnill, J. Buckeridge, S.A. Shevlin, A.J. Logsdail, S.M. Woodley, C.R.A. Catlow, M.J. Powell, R.G. Palgrave, I.P. Parkin, G.W. Watson, T.W. Keal, P. Sherwood, A. Walsh, A.A. Sokol, *Nat. Mater.*, 12 (2013) 798.
46. X.H. Li, M. Antonietti, *Chem. Soc. Rev.*, 42 (2013) 6593.
47. B.P. Sankapal, D.B. Salunkhe, S. Majumder, D.P. Dubal, *Rsc Adv.*, 6 (2016) 83175.
48. H. Li, Y.H. Li, M. Wang, Z. Niu, X.T. Wang, B.R. Hou, *Nanotechnology*, 29 (2018) 435706.
49. Y. Yang, Y.F. Cheng, *Electrochim. Acta*, 253 (2017) 134.
50. Y. Bu, Z. Chen, J. Ao, J. Hou, M. Sun, *J. Alloy. Compd.*, 731 (2018) 1214.
51. H. Li, X.T. Wang, L. Zhang, B.R. Hou, *Corros. Sci.*, 94 (2015) 342.
52. J. Zhang, J. Hu, Y.F. Zhu, Q. Liu, H. Zhang, R.G. Du, C.J. Lin, *Corros. Sci.*, 99 (2015) 118.
53. Ning X.B., S.S. Ge, X.T. Wang, H. Li, X.R. Li, X.Q. Liu, Y.L. Huang, *J. Alloy. Compd.*, 719 (2017) 15.